RSC Advances

PAPER

View Article Online
View Journal | View Issue

Cite this: *RSC Adv.*, 2024, **14**, 18685

Bandgap regulation and doping modification of $Ga_{2-x}Cr_xSe_3$ nanosheets†

Huan Yang,[ab] Yue Wu,[ab] Huirong Li,[ab] Yiwen Zhang,[ab] Linmei Gao,[ab] Lanfang Wang[ab] and Fang Wang *[ab]

Received 23rd April 2024
Accepted 4th June 2024

DOI: 10.1039/d4ra03028a

rsc.li/rsc-advances

Ga_2Se_3, an important direct wide bandgap semiconductor with excellent optoelectronic properties, has wide application potential in the fields of photodetectors, photoelectric sensors and solar cells. Herein, we describe the synthesis of Ga_2Se_3 semiconductor nanoparticles using a high temperature organic liquid phase method. Post-annealing treatment at different temperatures can not only improve the crystallinity of Ga_2Se_3 nanoparticles, but also regulate its optical band gap ranging from 2.50 to 2.80 eV. We further synthesized $Ga_{2-x}Cr_xSe_3$ nanosheets by doping $CrCl_3 \cdot 6H_2O$ in the reaction process. By adjusting the Cr doping concentration, $Ga_{2-x}Cr_xSe_3$ nanosheets can achieve a continuously tunable band gap in the range of 2.23 eV to 2.42 eV. Both $Ga_{2-x}Cr_xSe_3$ nanosheets and Ga_2Se_3 nanoparticles exhibit excellent and stable photoelectric switching performance. With Cr doping, $Ga_{2-x}Cr_xSe_3$ exhibits reduced Nyquist impedance and enhanced electrocatalytic activity, which is attributed to its ultrathin nanosheet morphology and large specific surface area. In addition, the diamagnetic behavior of pure Ga_2Se_3 changes to ferromagnetism with different Cr doping concentrations, and its magnetization is as high as 18.0 emu g^{-1} at $x = 0.4$. These findings demonstrate that $Ga_{2-x}Cr_xSe_3$ nanosheets have significant potential in future optoelectronic and magnetoelectric applications.

1. Introduction

Band engineering is an important tool for modulating the electronic structure of semiconductor materials and studying their physical properties. Current strategies for bandgap manipulation primarily include surface modification, doping/alloying, applying strain, constructing heterojunctions, *etc.*[1–4] These approaches can effectively alter the band structure of semiconductor materials, thereby affecting their electron transport, optical properties, and chemical activity.[5,6] Therefore, controlling the bandgap of semiconductors through various physical or chemical methods is essential for meeting specific application requirements.

China is the world's largest producer of Ga and Ge, and its Ga reserves rank first in the world.[7–9] III–VI compounds such as NX (N = Ga, In, and X = S, Se) have been enthusiastically studied due to their scientific merits of strong light absorption, high carrier mobility, flexibility, ultrathinness, larger area and thickness-tunable band gap modulation.[10–13] Ga_2Se_3 is a typical III_2VI_3 natural defective semiconductor, which crystallizes in a defect zincblende blende structure with one-third of cationic vacancy.[14–16] Ga_2Se_3 is a p-type semiconductor with a wide bandgap of 2.5 eV and has excellent photoelectric performances with a high photosensitivity (9.2 A W^{-1}) and a fast response time (rise/fall time of <4/3 ms).[17–20] And the constituents of Ga and Se are also low cost, nontoxic, and environmental friendly.[21,22] Thus, Ga_2Se_3 is attractive in next-generation high performance photodetection and photovoltaic.

In this work, defective Ga_2Se_3 nanoparticles and Cr-doped Ga_2Se_3 nanosheets were synthesized by a simple high temperature organic liquid phase method and their photoelectric response behavior and magnetic properties were systematically explored. Annealing treatment at different temperatures not only improved the crystallinity of Ga_2Se_3, but also finely tuned its optical band gap ranging from 2.50 to 2.80 eV. Meanwhile, Cr doping not only effectively adjusted the bandgap but also enhanced the material's magnetization performance and electrocatalytic activity. The $Ga_{2-x}Cr_xSe_3$ nanosheets demonstrated an adjustable band gap ranging from 2.23 to 2.42 eV. At a Cr concentration of $x = 0.4$, these nanosheets showed a significant magnetization intensity of up to 18.0 emu g^{-1} and exhibited excellent and stable photoelectric switching performance. Furthermore, $Ga_{1.6}Cr_{0.4}Se_3$

[a]School of Chemistry and Materials Science of Shanxi Normal University, Key Laboratory of Magnetic Molecules and Magnetic Information Materials of Ministry of Education, Taiyuan 030032, China. E-mail: wf_0716@163.com

[b]Research Institute of Materials Science of Shanxi Normal University, Collaborative Innovation Center for Advanced Permanent Magnetic Materials and Technology of Ministry of Education, Taiyuan 030032, China

† Electronic supplementary information (ESI) available. See DOI: https://doi.org/10.1039/d4ra03028a

nanosheets displayed reduced Nyquist impedance and enhanced electrocatalytic activity, which can be attributed to their ultrathin morphology and large specific surface area compared to the Ga_2Se_3 nanoparticles. Thus, the $Ga_{2-x}Cr_xSe_3$ nanosheets are promising for the next-generation diverse optoelectronic and magnetoelectric applications.

2. Experimental

2.1. Materials

Gallium acetylacetonate [$Ga(acac)_3$, 99.99%], chromium trichloride hexahydrate ($CrCl_3 \cdot 6H_2O$, 98%), selenium powder (Se, 200 mesh, 99.999%), oleylamine (OLA, 80–90%) and octadecylene (ODE) were purchased from Alfa Aesar. Ethanol (99.7%) was purchased from Tianjin Kermel, and hexane (99.5%) was obtained from Tianjin Fengchuan Chemical Reagent Co. All chemicals and solvents were used as received without any further purification.

2.2. Synthesis

0.5 mmol $Ga(acac)_3$, 1.0 mmol Se and solvents (OLA/ODE, 20 ml) added into a four-neck round-bottom flask at room temperature, sealed, and then degassed at 120 °C for 20 min with N_2 atmosphere. Then the mixture was heated up to 200 °C at the rate of ~2 °C min^{-1}, and allowed to be aged for another 2 h at this temperature in N_2 atmosphere. Finally, the solution was cooled down to room temperature naturally, and excess ethanol was added to precipitate the products, which can be harvested through centrifugation at 8000 rpm for 5 min. The Ga_2Se_3 nanoparticles can be obtained by rewashing the precipitates with ethanol and hexane for three times. And the $Ga_{2-x}Cr_xSe_3$ ($x = 0.2$, 0.4, 0.6) nanosheets were synthesized by adding $CrCl_3 \cdot 6H_2O$ (0.05 mmol, 0.10 mmol, 0.15 mmol) under the similar synthesis conditions.

2.3. Analysis and characterizations

The phase structures were identified by using powder X-ray diffraction (XRD, D8 Advance) with a Cu Kα radiation source ($\lambda = 0.154$ nm). The morphologies and element valences were investigated by scanning electron microscope (SEM, JSM-7500F), transmission electron microscope (TEM, JEM-F2100) equipped with energy-dispersive X-ray spectroscope (EDX), and X-ray photoelectron spectrometer (XPS, Thermo Scientific K-Alpha). The magnetic hysteresis loops (M–H) were performed using a physical property measurement system (PPMS, QD Dyna Cool) with a field of up to 5 T. The N_2 adsorption/desorption isotherms and pore size distribution curves were obtained by Micromeritics ASAP 2020. And all the electrochemical

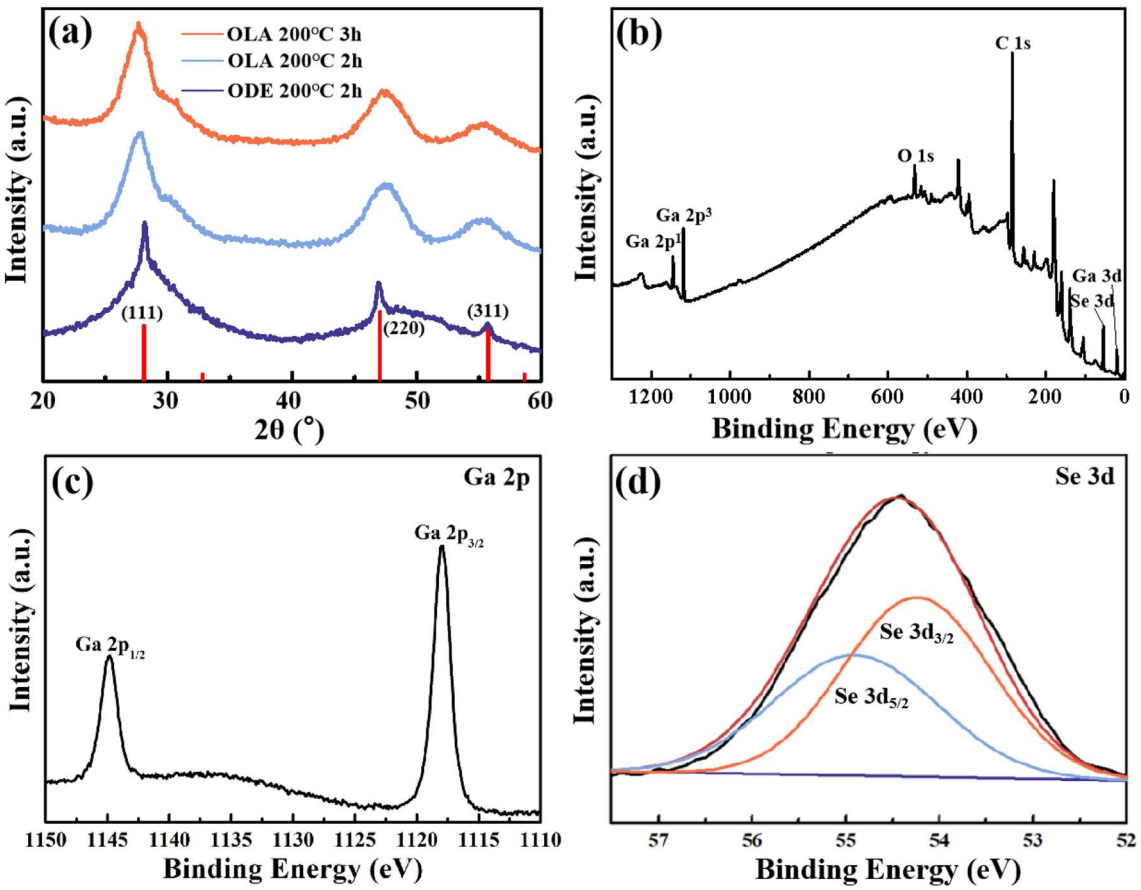

Fig. 1 (a) XRD patterns, (b–d) XPS spectra and high-resolution Ga 2p, Se 3d spectra of Ga_2Se_3 nanoparticles.

measurements were carried out on a CHI 660E electrochemical workstation (CH Instruments, Inc., Shanghai) with a standard three-electrode setup.

2.4. Electronic structure calculations

The theoretical calculations were based on density functional theory (DFT). The exchange–correlation potential of Perdew–Burke–Ernzerhof (PBE) with the generalized-gradient approximation (GGA) was used for structural relaxations of Ga_2Se_3 unit cell. The energy band structures and density of states (DOS) of original Ga_2Se_3, expand Ga_2Se_3 and $Ga_{2-x}Cr_xSe_3$ were performed with HSE06 functional.

3. Results and discussions

Colloidal Ga_2Se_3 nanoparticles were synthesized by a facile high temperature organic liquid phase method, employing gallium acetylacetonate and selenium in various solvents and at different reaction times. As depicted in Fig. 1a, all of the diffraction peaks could be indexed to the cubic Ga_2Se_3 (JCPDS 05-0724), revealing that the as-synthesized Ga_2Se_3 sample is a pure phase. XPS was utilized to further analyze the elemental compositions and chemical states of the Ga_2Se_3 nanoparticles. Low-resolution XPS survey confirms the presence of Ga, Se, O and C signals in Ga_2Se_3 sample (Fig. 1b). The observed oxygen peak can be attributed to the adsorption of air on the sample surface. In the magnified Ga-2p spectrum (Fig. 1c), two peaks located at 1144.8 eV and 1117.9 eV correspond with the Ga $2p_{1/2}$ and $2p_{3/2}$ of Ga^{3+}.[23,24] By fitting the Se-3d spectrum (Fig. 1d), the characteristic peaks at 55.1 eV and 54.2 eV correspond with the Se $3d_{3/2}$ and $3d_{5/2}$ binding energies of Se^{2-}, agreeing well with previous reports.[25] Moreover, the representative SEM images are shown in Fig. 2a–c, Ga_2Se_3 exhibit as highly uniform irregular nanoparticles with a diameter of about 500 nm. The TEM image and corresponding elemental mappings in Fig. 2d reveal that colocalization of the Ga and Se elements on the Ga_2Se_3 nanoparticles with an average atomic ratio of 38.18% : 61.82% (2 : 3) (Fig. 2e), in good agreement with the above XRD results.

Although Ga_2Se_3 pure phase has been prepared, it exhibits a wide diffraction peak (Fig. 1a). To further improve the crystallinity of Ga_2Se_3, the synthesized samples were annealed under vacuum conditions at temperatures of 150 °C, 200 °C, 250 °C, and 300 °C for 2 h. The XRD results (Fig. 3a) show that

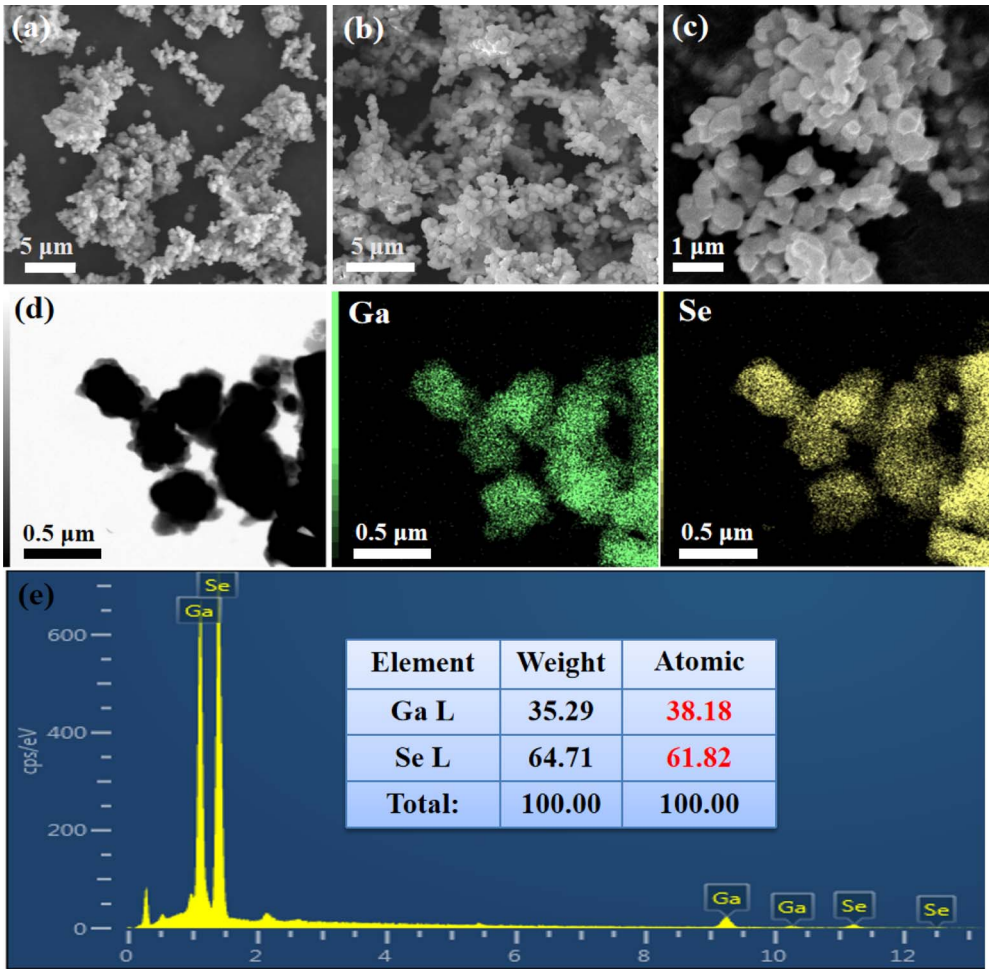

Fig. 2 (a–c) SEM images, (d) corresponding TEM elemental mappings and (e) EDX spectrum of the as-prepared Ga_2Se_3 nanoparticles.

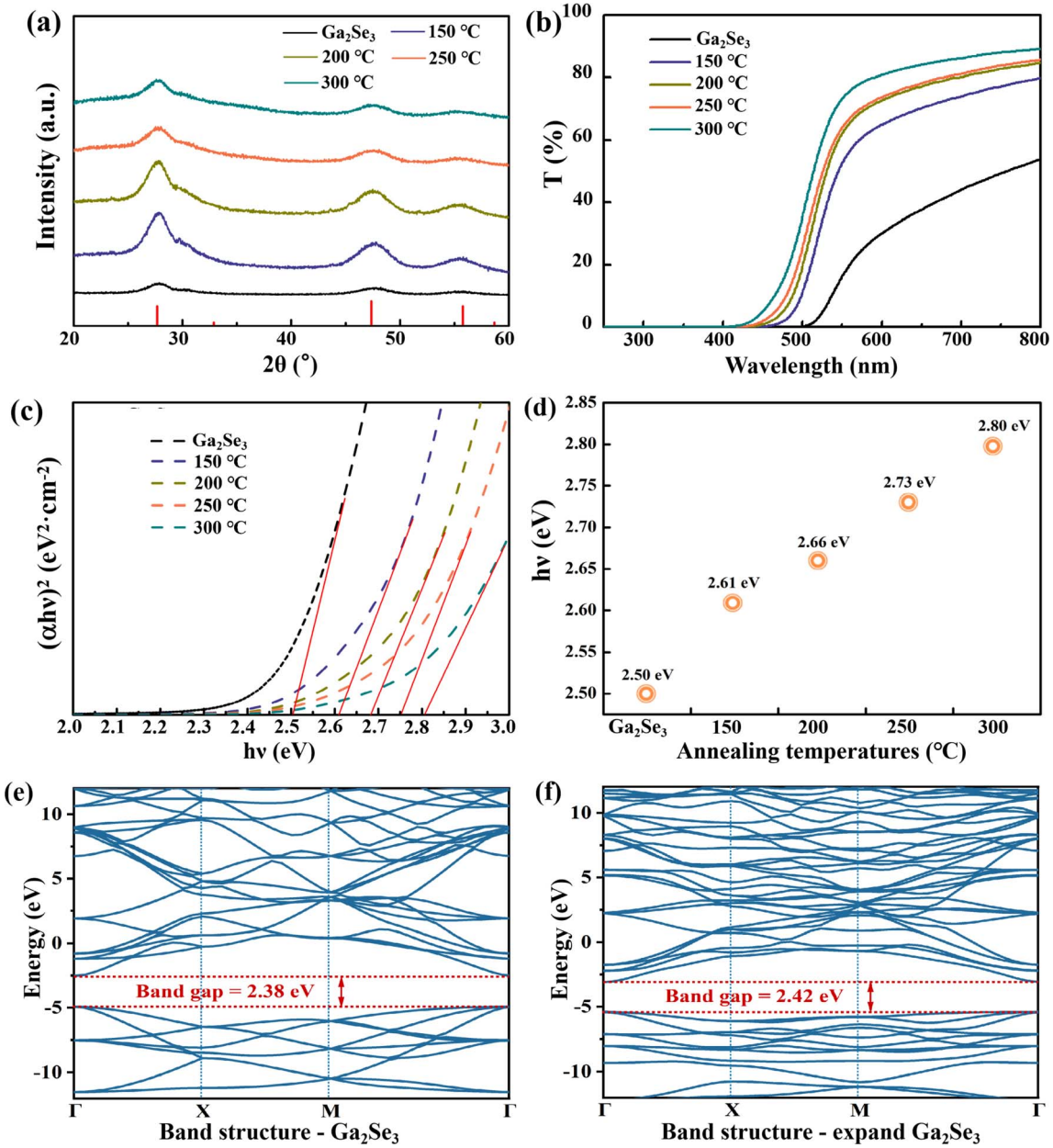

Fig. 3 (a) XRD patterns, (b) transmission spectra, (c) $(\alpha h\nu)^2$–$h\nu$ curves and (d) band gap values of Ga_2Se_3 sample at different annealing temperatures. (e and f) Calculated energy band structures of Ga_2Se_3 and expand Ga_2Se_3 using HSE06 functional.

the main peaks of Ga_2Se_3 are still present and without any impurities are observed, which further confirms that the Ga_2Se_3 samples did not undergo phase transformation after annealing. Post-annealing promotes the diffusion of atoms within a material, leading to an orderly realignment of atomic structures. This process effectively reduces grain boundaries and defects.[26] As a result, the crystallinity of Ga_2Se_3 samples is significantly improved after undergoing annealing. Notably, the sample annealed at 200 °C has the strongest XRD diffraction peak intensity, followed by a decrease in peak intensity with increasing annealing temperature. This suggests that the grain growth may be effectively promoted at 200 °C. Next, to further clarify the changes in XRD diffraction peaks after annealing, the thermal stability of the Ga_2Se_3 sample was carried out (Fig. S1†). From the thermogravimetric curve of Ga_2Se_3, weight loss is observed starting around about 200 °C, which is consistent with the decomposition temperature of selenium.[27] Moreover, upon annealing at 300 °C, the weight of Ga_2Se_3 nanoparticles decreases to 80% of the initial mass. Consequently, the decrease in peak intensity beyond 200 °C can be ascribed to the formation of selenium vacancies and the concomitant reduction in Ga_2Se_3 mass.

The optical bandgaps of Ga_2Se_3 samples were determined by UV-vis-NIR transmission spectra, as shown in Fig. 3b. The

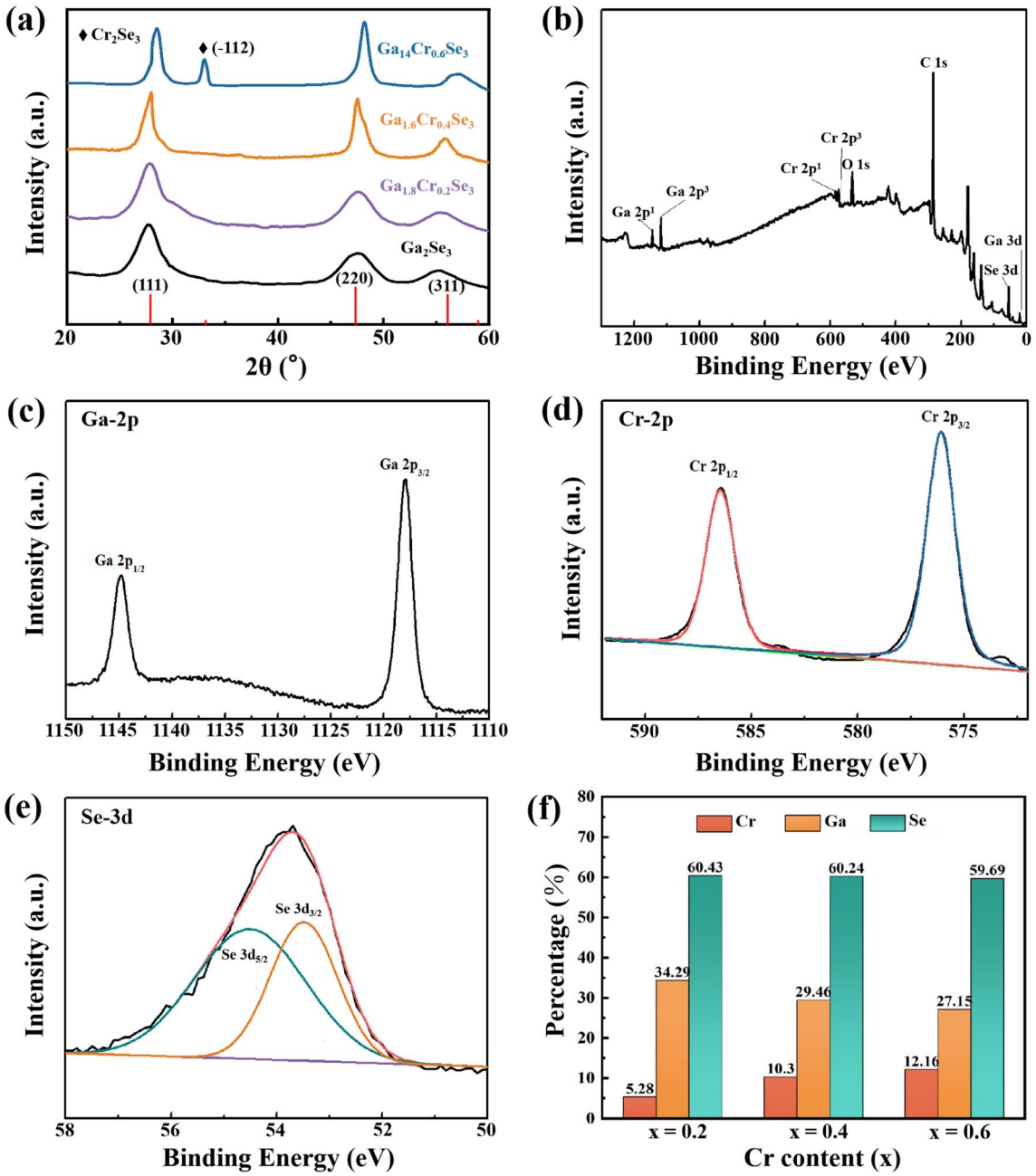

Fig. 4 (a) XRD patterns of different Cr-doped Ga_2Se_3 nanomaterials. (b) XPS spectra and (c–e) high-resolution spectra of Cr 2p, Ga 2p and Se 3d in $Ga_{1.6}Cr_{0.4}Se_3$ sample. (f) EDX analyses of $Ga_{2-x}Cr_xSe_3$ ($0 \leq x \leq 0.6$) with different Cr concentrations.

transmittance of Ga_2Se_3 nanoparticles had a sharply decline at about 570 nm and decreased almost to zero near 400 nm. And the absorption band edge of Ga_2Se_3 samples are continuously bule-shifted with increasing annealing temperatures. The bandgap was calculated according to the equation $(\alpha hv)^n = C(hv - E_g)$, where C is a constant, α is the absorption coefficient, E_g is band gap, hv is the photon energy and n equals to 2 for direct inter-band transition.[28] By plotting $(\alpha hv)^2$–hv curves (Fig. 3c) and extrapolating the linear sections of the curves to the x-axis, the band gaps were determined to be 2.50, 2.61, 2.66, 2.73, and 2.80 eV for the untreated and annealed samples at 150, 200, 250, and 300 °C, respectively (Fig. 3d). Table S1† shows the lattice constants and cell volumes calculated from the XRD patterns in Fig. 3a. It is observed that annealing at various temperatures leads to a large lattice constant (a) compared to the original Ga_2Se_3. The non-monotonic increase

in lattice constants (a) at 250 °C may be attributed to lattice distortion effects. And the lattice distortion relative to Ga_2Se_3 for annealing at 150, 200, 250, and 300 °C is $\Delta V = 3.46$, 4.85, 3.37 and 4.40 Å^3. At high temperatures, atomic or phonon vibrations significantly affect the band gap through electron–phonon interactions and lattice thermal expansion, as observed in semiconductors like black phosphorus and $CsSnI_3$.[29,30] To further investigate the influence of lattice parameters and chemical bonds on the band gap of Ga_2Se_3, we conducted first-principles calculations. As depicted in the band structure in Fig. 3e, the untreated Ga_2Se_3 has a band gap of 2.38 eV, which is a direct band gap material due to the alignment of the valence band maximum and conduction band minimum at the same high-symmetry point. As the lattice constant of Ga_2Se_3 increases from 5.219 Å to 5.438 Å, the lattice expansion weakens the interaction between atoms, resulting in a decrease in the overlap of Ga and Se atomic orbitals (Fig. 3f). This separation of electronic states in the valence band and conduction band leads to an increase in the band gap to 2.42 eV.

Fig. 4a shows the XRD patterns of different Cr-doped Ga_2Se_3 nanomaterials. The main peaks (111) and (220) of Ga_2Se_3 shift

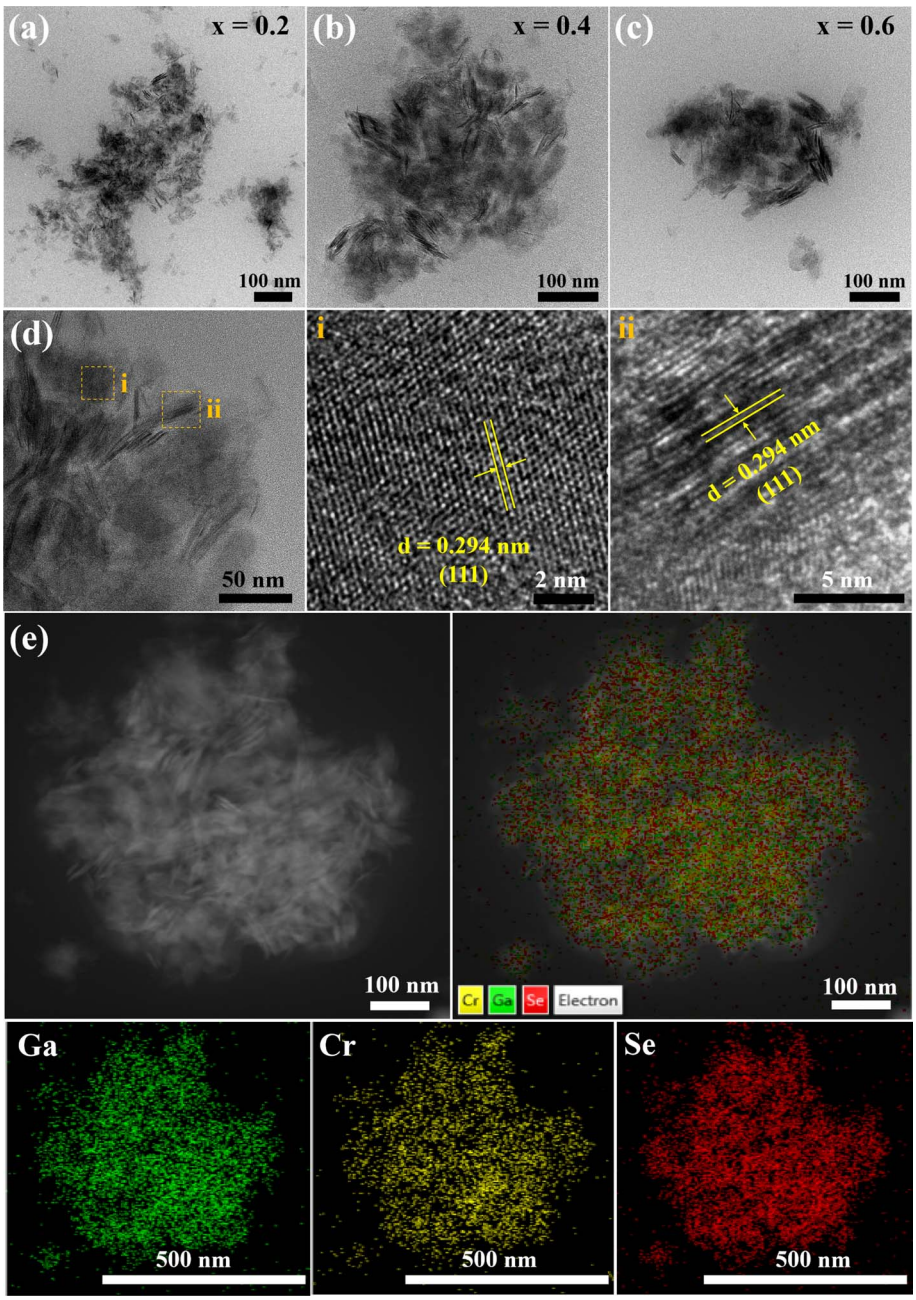

Fig. 5 (a–c) TEM images of $Ga_{2-x}Cr_xSe_3$ ($0 \le x \le 0.6$) nanosheets with different Cr concentrations. (d) Enlarged TEM, HRTEM and (e) corresponding elemental mappings images of $Ga_{1.6}Cr_{0.4}Se_3$ nanosheets.

to the higher angle with increasing Cr dopant content ($0 < x \leq 0.6$), which is attributed to the replacement of Cr^{3+} (69 pm) by the smaller Ga^{2+} (62 pm). And the corresponding lattice constants and unit cell volumes of the $Ga_{2-x}Cr_xSe_3$ were summarized in Table S2.† However, when the Cr doping content reaches 0.6, the diffraction peak at 33° can correspond to the hexagonal Cr_2Se_3 (−112) crystal plane. These results indicate that Cr ions can be successfully doped into Ga_2Se_3 lattice, while the excessive Cr ions will combine with Se ions to form new phase Cr_2Se_3. XPS spectra (Fig. 4b) further confirm the presence of Ga, Se and Cr in the $Ga_{2-x}Cr_xSe_3$ ($x = 0.4$) sample. From Cr-3d spectrum in Fig. 4c, the chemical states of Cr $2p_{1/2}$ and $2p_{3/2}$ can be identified from the peaks at binding energies of 586.5 eV and 576.2 eV, which proves the sample is indeed doped with Cr element.[31] And the Ga-2p and Se-3d spectra in $Ga_{2-x}Cr_xSe_3$ ($x = 0.4$) are the same as those in Ga_2Se_3 (Fig. 4d and e). The content of Cr, Ga and Se elements in $Ga_{2-x}Cr_xSe_3$ samples was analyzed using EDX spectra, as shown in Fig. S3 and Table S3.† The histogram in Fig. 4 signifies that as the doping amount (x) increases, the amount of chromium gradually increases, while the content of gallium gradually decreases. Significantly, the total cation content (Cr^{3+} + Ga^{3+}) and the total anion content (Se^{2-}) maintained a constant ratio of 2 : 3. This further confirms the partial substitution of Ga cations by Cr cations, indicating a substitutional doping has occurred between cations.

Fig. 5 shows TEM images of $Ga_{2-x}Cr_xSe_3$ with different Cr dopants. All $Ga_{2-x}Cr_xSe_3$ samples are composed of ultra-thin nanosheets with a size of about 100 nm and are well dispersed (Fig. 5a–c). In the high-resolution TEM image of the $Ga_{1.6}Cr_{0.4}Se_3$ sample (Fig. 5d), a clear lattice fringe of 0.294 nm is observed, which is smaller than the lattice spacing (0.314 nm) on the (111) plane of cubic Ga_2Se_3. It is consistent that the (111) peak has a slight blueshift in the XRD pattern. The elements Cr, Ga and Se are uniformly distributed in $Ga_{1.6}Cr_{0.4}Se_3$ ultra-thin nanosheets (Fig. 5e). Thus, Cr doping in Ga_2Se_3 facilitates the formation of ultrathin nanosheets.

The magnetic hysteresis loops (Fig. 6a) of $Ga_{2-x}Cr_xSe_3$ ($0 \leq x \leq 0.6$) at 5 K were obtained by PPMS. When $x = 0$, Ga_2Se_3 nanoparticles show a diamagnetic signal. The M–H curve is a straight line passing through the second and fourth quadrants, and the magnetic moment is almost 0. As the incorporation of Cr ions into the Sb_2Se_3 lattice, the system began to exhibit ferromagnetism. When $x = 0.4$, the magnetization can reach up to 18.0 emu g^{-1} at 40 kOe. The 3d orbital partially occupied by Cr element is the main magnetic moment source. However, when the Cr content increases to $x = 0.6$, the system exhibits antiferromagnetism. This is consistent with the reported antiferromagnetism of Cr_2Se_3 nanostructures with

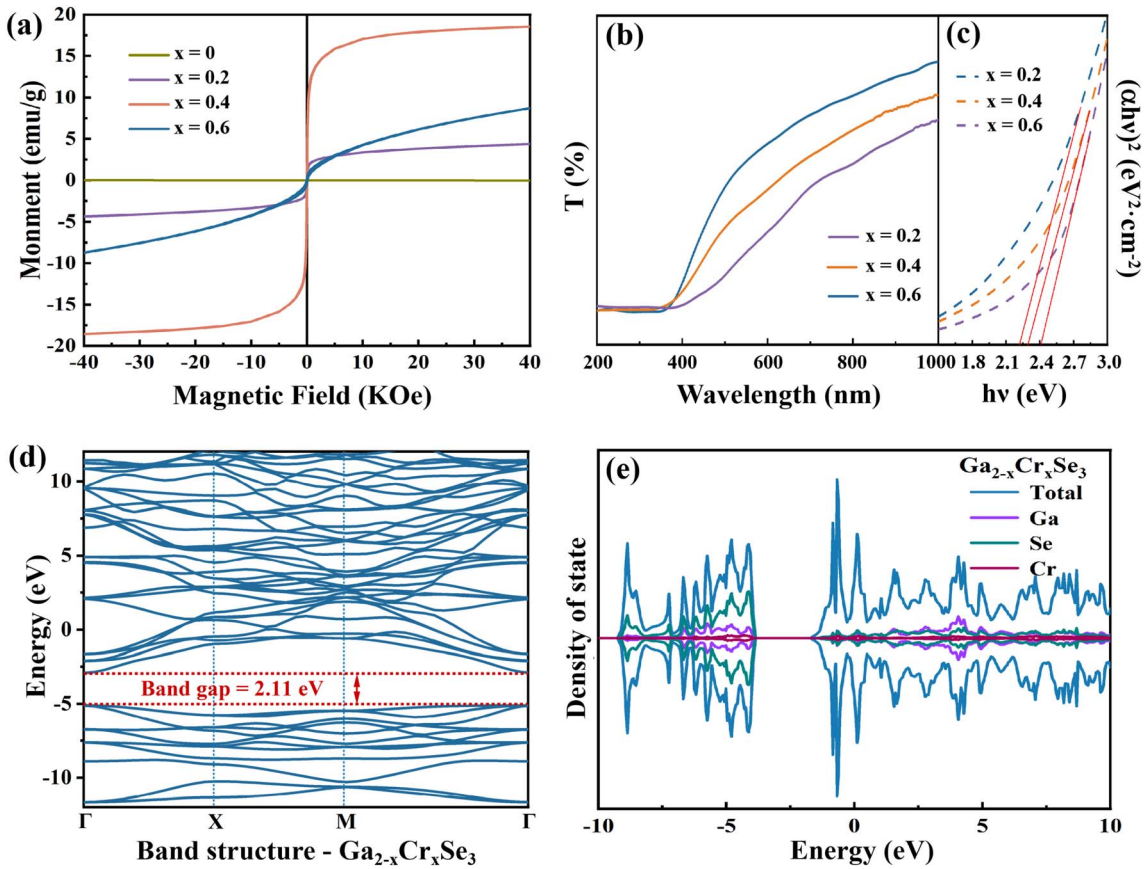

Fig. 6 (a) M–H loops measured at 5 K, (b) transmission spectra, (c) $(\alpha h\nu)^2$–$h\nu$ curves of the $Ga_{2-x}Cr_xSe_3$ ($0 \leq x \leq 0.6$) nanosheets with different Cr concentrations. (d and e) Calculated energy band structure and DOS plot of $Ga_{2-x}Cr_xSe_3$ sample.

non-collinear spin configuration, which confirms the XRD results.

Cr doping not only induces ferromagnetism in $Ga_{2-x}Cr_xSe_3$ system, but also affects the band gaps of Ga_2Se_3. From the transmission curves and plotting $(\alpha h\nu)^2$–$h\nu$ curves (Fig. 6b and c), it can be seen that the band gaps of $Ga_{2-x}Cr_xSe_3$ are estimated as 2.42, 2.30, and 2.23 eV when the Cr content (x) is 0.2, 0.4 and 0.6. The introduction of Cr ions significantly alters the electronic structure of Ga_2Se_3. The detailed analysis of the band structure and DOS calculations demonstrates that the newly introduced Cr ion density peaks appear near the Fermi level, increasing the density of states around this region. This increase reduces the energy required for electrons to transition from the valence band to the conduction band, resulting in a decrease in the band gap of $Ga_{2-x}Cr_xSe_3$ (2.11 eV). Combined with the band gaps of Ga_2Se_3 annealed at different temperatures (2.50–2.80 eV), the band gaps of the $Ga_{2-x}Cr_xSe_3$ nanomaterials can achieve continuous changes in the range of 2.23 eV to 2.80 eV.

The photoelectrochemical performances of Ga_2Se_3 and $Ga_{2-x}Cr_xSe_3$ ($x = 0.4$) were investigated through the hydrogen evolution reaction (HER) in 0.5 mol per L H_2SO_4 aqueous solution. The LSV curves of both Ga_2Se_3 and $Ga_{1.6}Cr_{0.4}Se_3$ (Fig. S4†) show positive response to simulated light (a 300 W Xe lamp) in the range of 0 to −0.6 V. Notably, the doped $Ga_{1.6}Cr_{0.4}Se_3$ always displays superior onset potentials for HER compared to pure Ga_2Se_3 in both light and dark conditions. I–t curves in Fig. 7a and b further indicate the Ga_2Se_3 and $Ga_{1.6}Cr_{0.4}Se_3$ have good photocurrent response in the whole 600 s switching visible light on/off cycle. And the photocurrent densities could be effectively modulated by varying the bias voltage. Specifically, the photocurrent density of $Ga_{1.6}Cr_{0.4}Se_3$ increased from 0.2 to 15.5 mA cm^{-2}, with the applied bias potentials increasing from −0.2 to −0.6 V, respectively. This enhancement is attributed to the role of bias potentials in facilitating the separation and migration rate of photogenerated electron–hole pairs. Additionally, the lower impedance and charge transfer resistance of $Ga_{1.6}Cr_{0.4}Se_3$, confirmed by EIS measurements (Fig. 7c and d), suggest that a certain amount of Cr doping significantly improves photoelectrocatalytic hydrogen evolution performance. Additional N_2 adsorption/desorption isotherms (Fig. 8a and b) display typical type IV behavior according to the IUPAC classification, and pore size distribution curves (Fig. 8c and d) confirm that both materials are primarily mesoporous. Notably, the BET surface area of $Ga_{1.6}Cr_{0.4}Se_3$ was measured at 39.1 $m^2\ g^{-1}$, significantly higher than the 7.9 $m^2\ g^{-1}$ recorded for Ga_2Se_3 (Table S4†). The large surface area should favor the rapid transfer of electrons during photoelectrocatalytic processes, which is consistent with the catalytic results.

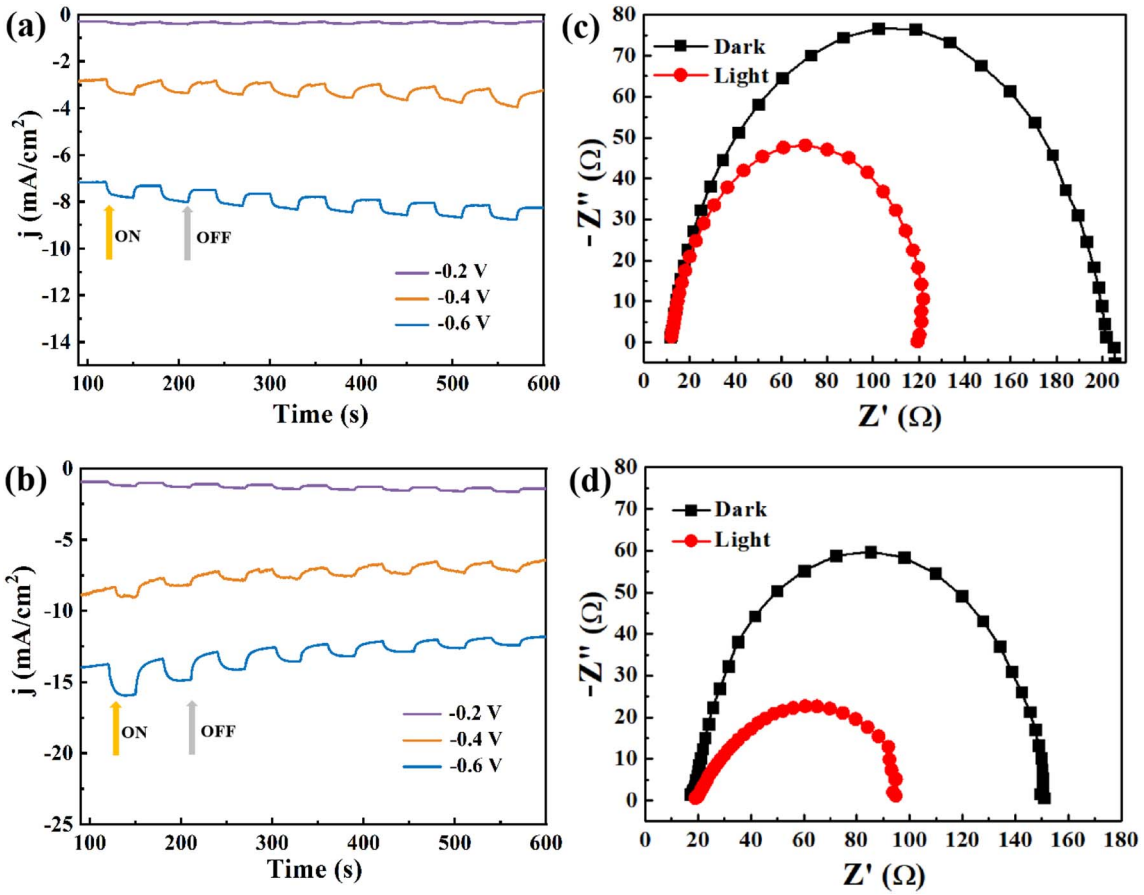

Fig. 7 (a and b) I–t curves and (c and d) EIS curves of Ga_2Se_3 nanoparticles and $Ga_{1.6}Cr_{0.4}Se_3$ nanosheets.

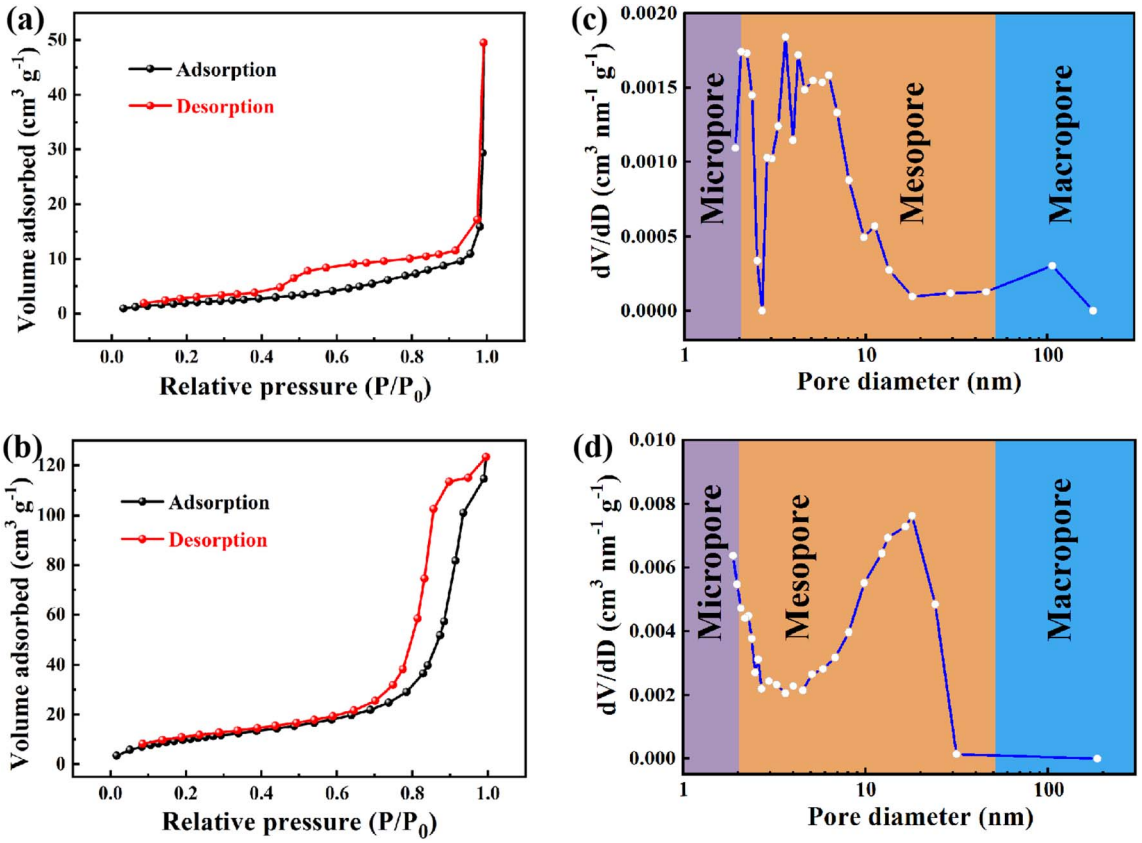

Fig. 8 (a and b) N_2 adsorption/desorption isotherms and (c and d) the corresponding pore-size distribution curves of Ga_2Se_3 nanoparticles and $Ga_{1.6}Cr_{0.4}Se_3$ nanosheets.

4. Conclusion

In summary, we have successfully synthesized Ga_2Se_3 nanoparticles and $Ga_{2-x}Cr_xSe_3$ nanosheets using high temperature organic liquid phase method. The optical band gaps of $Ga_{2-x}Cr_xSe_3$ can be continuously adjusted in the range of 2.23 to 2.80 eV with changing the annealing temperature (150–300 °C) and introduction of different Cr doping concentrations. The magnetic study results indicate that moderate Cr doping ($x < 0.4$) induces a transition in Ga_2Se_3 from paramagnetic to ferromagnetic behavior, with a magnetization intensity reaching 18.0 emu g^{-1} at 40 kOe. Besides, photoelectrochemical studies reveal that $Ga_{1.6}Cr_{0.4}Se_3$ nanosheets exhibit superior hydrogen evolution performance compared to Ga_2Se_3 nanoparticles. Therefore, the dual modulation of bandgap and magnetic properties through Cr doping presents a promising avenue for the development of high-performance opto-electromagnetic devices.

Data availability

The data that support the findings of this study are available from the corresponding author upon reasonable request.

Conflicts of interest

There is no conflict to declare.

Acknowledgements

This work was supported by the National Natural Science Foundation of China (52301244, 52371191, 52202340) and the Youth Science Foundation of Shanxi Province (202203021222218).

References

1 H. Kim, D. Monllor-Satoca, W. Kim and W. Choi, *Energy Environ. Sci.*, 2015, **8**, 247–257.
2 Q. Deng, X. Li, H. Si, J. Hong, S. Wang, Q. Feng, C. X. Hu, S. Wang, H. L. Zhang, K. Suenaga and H. Xu, *Adv. Funct. Mater.*, 2020, **30**, 2003264.
3 Z. Dai, L. Liu and Z. Zhang, *Adv. Mater.*, 2019, **31**, 1805417.
4 Q. Lv and R. Lv, *Carbon*, 2019, **145**, 240–250.
5 M. Kapilashrami, Y. Zhang, Y. S. Liu, A. Hagfeldt and J. Guo, *Chem. Rev.*, 2014, **114**, 9662–9707.
6 J. H. Clark, M. S. Dyer and R. G. Palgrave, *J. Am. Chem. Soc.*, 2011, **133**, 1016–1032.
7 S. Dai, X. Yan, C. R. Ward, J. C. Hower, L. Zhao, X. Wang, L. Zhao, D. Ren, and R. B. Finkelman, *Coal Geology of China*, Area Studies, London, 2020.
8 Z. Lu, G. P. Neupane, G. Jia, H. Zhao, D. Qi, Y. Du, Y. Lu and Z. Yin, *Adv. Funct. Mater.*, 2020, **30**, 2001127.

9 K. Xu, L. Yin, Y. Huang, T. A. Shifa, J. Chu, F. Wang, R. Cheng, Z. Wang and J. He, *Nanoscale*, 2016, **8**, 16802–16818.
10 X. Li, L. Li and M. Wu, *Mater. Today Phys.*, 2020, **15**, 100229.
11 N. Balakrishnan, Z. R. Kudrynskyi, M. W. Fay, G. W. Mudd, S. A. Svatek, O. Makarovsky, Z. D. Kovalyuk, L. Eaves, P. H. Beton and A. Patanè, *Adv. Opt. Mater.*, 2014, **2**, 1064–1069.
12 H. Cai, Y. Gu, Y. C. Lin, Y. Yu, D. B. Geohegan and K. Xiao, *Appl. Phys. Rev.*, 2019, **6**, 041312.
13 C. H. Ho, X. R. Lai, C. A. Chuang, W. L. Kuo and K. K. Tiong, *Adv. Photonics Res.*, 2021, **2**, 2000110.
14 W. Xue, Q. Jiang, F. Wang, R. He, R. Pang, H. Yang, P. Wang, R. Yang, Z. Zhong, T. Zhai and X. Xu, *Small*, 2022, **18**, 2105599.
15 G. Y. Huang, N. M. Abdul-Jabbar and B. D. Wirth, *J. Phys.: Condens.Matter*, 2013, **25**, 225503.
16 M. Isik and N. M. Gasanly, *Vacuum*, 2020, **179**, 109501.
17 C. H. Ho, *ACS Omega*, 2020, **5**, 18527–18534.
18 C. A. Chuang, M. H. Lin, B. X. Yeh and C. H. Ho, *RSC Adv.*, 2018, **8**, 2733–2739.
19 A. Ravagli, C. Craig, G. A. Alzaidy, P. Bastock and D. W. Hewak, *Adv. Mater.*, 2017, **29**, 1606329.
20 G. Y. Huang, N. M. Abdul-Jabbar and B. D. Wirth, *Acta Mater.*, 2014, **71**, 349–369.
21 K. George, C. H. de Groot, C. Gurnani, A. L. Hector, R. Huang, M. Jura, W. Levason and G. Reid, *Chem. Mater.*, 2013, **25**, 1829–1836.
22 C. S. Jung, F. Shojaei, K. Park, J. Y. Oh, H. S. Im, D. M. Jang, J. Park and H. S. Kang, *ACS Nano*, 2015, **9**, 9585–9593.
23 T. Zhang, Y. Li, Y. Zhang, Q. Feng, J. Ning, C. Zhang, J. Zhang and Y. Hao, *J. Alloys Compd.*, 2021, **859**, 157810.
24 C. V. Ramana, D. Das, G. Gutierrez, F. S. Manciu and V. Shutthanandan, *J. Mater. Sci.*, 2022, **57**, 11170–11188.
25 H. Yang, Y. Wu, L. Y. Hu, J. J. Wang, F. Wang and X. H. Xu, *Rare Met.*, 2023, **42**, 189–197.
26 C. Kim, K. Kurosaki, M. Ishimaru, H. Muta and S. Yamanaka, *J. Electron. Mater.*, 2011, **40**, 999–1004.
27 D. Sun, S. Xu, L. Zhang, Z. Chen, Y. Ge, N. Wang, X. Liang, C. Wei, Y. Zhao and X. Zhang, *J. Semicond.*, 2015, **36**, 044009.
28 J. I. Pankove, *Optical Processes in Semiconductors*, Courier Corporation, 1975.
29 C. E. P. Villegas, A. R. Rocha and A. Marini, *Nano Lett.*, 2016, **16**, 5095–5101.
30 C. Yu, Z. Chen, J. J. Wang, W. Pfenninger, N. Vockic, J. T. Kenney and K. Shum, *J. Appl. Phys.*, 2011, **110**, 063526.
31 H. Yang, F. Wang, H. Zhang, L. Guo, L. Hu, L. Wang, D. J. Xue and X. Xu, *J. Am. Chem. Soc.*, 2020, **142**, 4438–4444.